Postsynthetic Installation of Lanthanide Cubane Clusters in a 3D Hydrogen-Bonded Framework of $Ir^{III}_4Zn^{II}_4$ Multicarboxylates

Supaphorn Thammakan,[a] Nobuto Yoshinari,[a] Marie Tsuchikawa,[a] Apinpus Rujiwatra,[b,c] Takumi Konno[a,d]**

[a] Department of Chemistry, Graduate School of Science, Osaka University, Toyonaka, Osaka 560-0043, Japan

[b] Department of Chemistry, Faculty of Science, Chiang Mai University, Chiang Mai 50200, Thailand

[c] Materials Science Research Center, Faculty of Science, Chiang Mai University, 239 Huay Kaew Road, Chiang Mai 50200, Thailand

[d] Department of Chemistry, College of Science, National Taiwan Normal University, Taipei 11677, Taiwan

ABSTRACT: Immersing single crystals of $(\Delta)_4$-$K_6[Ir_4Zn_4O(\text{L-cysteinate})_{12}]\cdot n H_2O$ ($K_6[\mathbf{1^{Ir}}]\cdot n H_2O$) bearing 12 free carboxylate groups, which was newly prepared from Δ-$H_3[Ir(\text{L-cysteinate})_3]$, $ZnBr_2$, ZnO, and KOH, in an aqueous solution of lanthanide(III) acetate produced $Ln_2[\mathbf{1^{Ir}}]\cdot n H_2O$

(**2**$_{\mathbf{Ln}}$; Ln = La^{III}, Ce^{III}, Pr^{III}, and Nd^{III}) and $Ln_{0.33}[Ln_4(OH)_4(OAc)_3(H_2O)_7][\mathbf{1}^{\mathbf{Ir}}]\cdot nH_2O$ (**3**$_{\mathbf{Ln}}$; Ln = Sm^{III}, Eu^{III}, Gd^{III}, Tb^{III}, Dy^{III}, Er^{III}, Ho^{III}, Tm^{III}, Yb^{III}, and Lu^{III}) in a single-crystal-to-single-crystal transformation manner. X-ray crystallography showed that the K^I ions in $K_6[\mathbf{1}^{\mathbf{Ir}}]\cdot nH_2O$ are completely exchanged by the Ln^{III} ions in **2**$_{\mathbf{Ln}}$ and **3**$_{\mathbf{Ln}}$, retaining the 3D hydrogen-bonded framework that consists of the $Ir^{III}_4Zn^{II}_4$ complex anions of $[\mathbf{1}^{\mathbf{Ir}}]^{6-}$. While **2**$_{\mathbf{Ln}}$ contained the Ln^{III} ions as isolated aqua species, the Ln^{III} ions in **3**$_{\mathbf{Ln}}$ existed as cationic cubane clusters of $[Ln_4(OH)_4(OAc)_3(H_2O)_7]^{5+}$; these were linked by $[\mathbf{1}^{\mathbf{Ir}}]^{6-}$ anions through carboxylate groups in a 3D polymeric structure. **3**$_{\mathbf{Ln}}$ showed magnetic and photoluminescence properties that are characteristically observed for discrete Ln^{III} species in the solid state.

Introduction

Recent interest in the development of lanthanide clusters with bridging hydroxide groups, formulated as $Ln_x(OH)_y$, stems from their unique chemical and physical properties and their fascinating designs with the potential for a variety of applications.[1-3] In general, $Ln_x(OH)_y$ clusters with different compositions have been synthesized via the ligand-controlled hydrolytic approach, in which the degree of hydrolysis of Ln^{III} centers is controlled by supporting organic/inorganic ligands used in the reaction.[4-6] One of the representative clusters of this class is the tetranuclear $Ln_4(OH)_4$ with a cubane form.[6-25] While several supporting ligands, such as amino carboxylates,[6,10-13] aromatic carboxylates,[6,14-22] Schiff bases,[23] and β-diketonates,[24] have been used to produce $Ln_4(OH)_4$ cubanes via a ligand-controlled approach, their rational synthesis remains challenging due to the large pH dependency of hydrolysis and the flexibility of lanthanide coordination geometries.[4,5,25]

To overcome the limitation of the ligand-controlled approach, the use of interstitial spaces in coordination compounds is an alternative way to generate $Ln_4(OH)_4$ cubane clusters.[26-28] Recently, we reported that a series of $Ln_4(OH)_4$ cubanes are formed in the interstices of a 3D hydrogen-bonded framework consisting of $Rh^{III}_4Zn^{II}_4$ complex anions with 12 free carboxylate groups, $(\Delta)_4$-$[Zn_4O\{Rh(\text{L-cysteinate})_3\}_4]^{6-}$ ($[\mathbf{1}^{\mathbf{Rh}}]^{6-}$), just by immersing crystals of $K_6[\mathbf{1}^{\mathbf{Rh}}]\cdot n H_2O$ in an aqueous solution of $Ln(OAc)_3$.[29] In this process, the K^I ions in $K_6[\mathbf{1}^{\mathbf{Rh}}]\cdot n H_2O$ were completely exchanged with Ln^{III} ions such that the cubane structure of $Ln_4(OH)_4$ is spontaneously constructed in the hydrogen-bonded framework via single-crystal-to-single-crystal (SCSC) transformation. However, the construction of $Ln_4(OH)_4$ was limited to the late lanthanide ions of Gd^{III}, Tb^{III}, Dy^{III}, Er^{III}, Ho^{III}, Tm^{III}, Yb^{III}, and Lu^{III}, while the Ln^{III} ions existed in the framework as discrete aqua species for the early lanthanide ions of La^{III}, Ce^{III}, Pr^{III}, Nd^{III},

Sm^{III}, and Eu^{III}. This occurred because the interstitial space in the hydrogen-bonded framework of $[\mathbf{1}^{\mathbf{Rh}}]^{6-}$ is not large enough to accommodate these early lanthanide ions with larger ionic sizes in the cubane form of $Ln_4(OH)_4$. To expand the series of lanthanide ions that are accommodated in the framework in the cubane form, in this work, the $Ir^{III}_4Zn^{II}_4$ octanuclear complex analogous to $K_6[\mathbf{1}^{\mathbf{Rh}}]\cdot n H_2O$, $(\Delta)_4$-$K_6[Zn_4O\{Ir(\text{L-cysteinate})_3\}_4]\cdot n H_2O$ ($K_6[\mathbf{1}^{\mathbf{Ir}}]\cdot n H_2O$), was newly prepared to employ it for the cation-exchange reaction using $Ln(OAc)_3$ (Scheme 1). We found that not only Gd^{III} - Lu^{III} but also Sm^{III} and Eu^{III} could be accommodated in the 3D hydrogen-bonded framework of $[\mathbf{1}^{\mathbf{Ir}}]^{6-}$ in the $Ln_4(OH)_4$ cubane form, accompanied by the complete exchange of the K^I ions in $K_6[\mathbf{1}^{\mathbf{Ir}}]\cdot n H_2O$ by Ln^{III} ions in an SCSC transformation manner. The unique solid-state photoluminescence properties of the products, together with their magnetic properties, are also discussed.

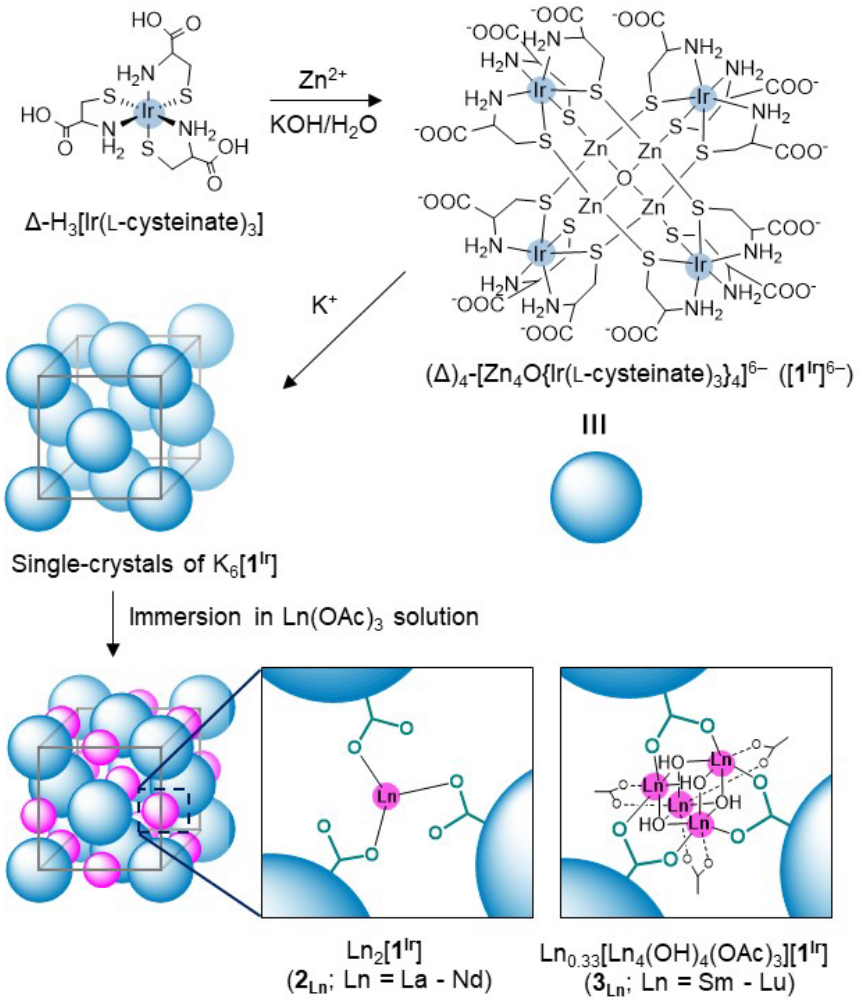

Scheme 1. Synthetic route of $K_6[\mathbf{1}^{Ir}]\cdot n H_2O$ and its conversion to $\mathbf{2}_{Ln}$ and $\mathbf{3}_{Ln}$. The H_2O molecules are omitted for clarity.

Experimental Section

Synthesis of (Δ)$_4$-K$_6$[Zn$_4$O{Ir(L-cysteinate)$_3$}$_4$]·nH$_2$O (K$_6$[1^{Ir}]·nH$_2$O)

To an off-white suspension containing 0.25 g (0.45 mmol) of Δ-H$_3$[Ir(L-cysteinate)$_3$] [30] in 10 mL of water were added 0.37 g (4.5 mmol) of ZnO and 0.22 g (0.98 mmol) of ZnBr$_2$ at room

temperature with stirring. The pH of the mixture was adjusted to ca. 9 using a 0.5 M aqueous solution of KOH, followed by stirring at room temperature for 3 h. After removing unreacted ZnO by filtration, a large amount of ethanol was added to the colorless filtrate. The resulting white solid was filtered and dried at room temperature. Yield: 0.22 g (65%). ^{1}H NMR (500 MHz, D_2O): δ 3.32 (dd, J = 12.9, 3.7 Hz, 1H), 2.84 (t, J = 12.5 Hz, 1H), 2.68 (dd, J = 11.7, 3.7 Hz, 1H). Anal. Calcd for $K_6[\mathbf{1^{Ir}}]\cdot 36H_2O = C_{36}H_{132}Ir_4K_6N_{12}O_{61}S_{12}$: C, 12.87; H, 3.96; N, 5.00. Found: C, 12.83; H, 3.89; N, 4.96.

Colorless crystals suitable for single-crystal X-ray crystallography were obtained by diffusing ethanol vapor into an almost saturated solution of $K_6[\mathbf{1^{Ir}}]\cdot nH_2O$ dissolved in a 0.1 M aqueous solution of KOAc.

Synthesis of $Ln_2[\mathbf{1^{Ir}}]\cdot n\mathbf{H_2O}$ ($\mathbf{2_{Ln}}$; Ln = $\mathbf{La^{III}}$, $\mathbf{Ce^{III}}$, $\mathbf{Pr^{III}}$, $\mathbf{Nd^{III}}$) and $Ln_{0.33}[Ln_4(OH)_4(OAc)_3(H_2O)_7][\mathbf{1^{Ir}}]\cdot n\mathbf{H_2O}$ ($\mathbf{3_{Ln}}$; Ln = $\mathbf{Sm^{III}}$, $\mathbf{Eu^{III}}$, $\mathbf{Gd^{III}}$, $\mathbf{Tb^{III}}$, $\mathbf{Dy^{III}}$, $\mathbf{Er^{III}}$, $\mathbf{Ho^{III}}$, $\mathbf{Tm^{III}}$, $\mathbf{Yb^{III}}$, $\mathbf{Lu^{III}}$)

Freshly prepared single crystals of $K_6[\mathbf{1^{Ir}}]\cdot nH_2O$ (ca. 50 mg) were immersed in a 0.02 M ethanol:water (3:1) solution of $Ln(OAc)_3$ (10 mL) in a sealed glass vessel; the mixture was allowed to stand at room temperature for one week. To complete the reaction, the solution was then changed to a 0.1 M aqueous solution of $Ln(OAc)_3$ (5 mL); this mixture remained at room temperature for 2 days. The resulting crystals were collected by filtration and then washed with water.

Anal. Calcd for $La_2[\mathbf{1^{Ir}}]\cdot 30H_2O$ ($\mathbf{2_{La}}$) = $C_{36}H_{120}La_2N_{12}O_{55}Ir_4S_{12}Zn_4$: C, 13.12; H, 3.67; N, 5.10%. Found: C, 13.09; H, 3.57; N, 4.98%.

Anal. Calcd for $Ce_2[\mathbf{1}^{Ir}]\cdot 29H_2O$ ($\mathbf{2}_{Ce}$) = $C_{36}H_{118}Ce_2N_{12}O_{54}Ir_4S_{12}Zn_4$: C, 13.18; H, 3.63; N, 5.13%. Found: C, 13.05; H, 3.52; N, 5.00%.

Anal. Calcd for $Pr_2[\mathbf{1}^{Ir}]\cdot 26H_2O$ ($\mathbf{2}_{Pr}$) = $C_{36}H_{112}Pr_2N_{12}O_{51}Ir_4S_{12}Zn_4$: C,13.42; H, 3.49; N, 5.20%. Found: C, 13.44; H, 3.39; N, 4.97%.

Anal. Calcd for $Nd_2[\mathbf{1}^{Ir}]\cdot 35H_2O$ ($\mathbf{2}_{Nd}$) = $C_{36}H_{130}Nd_2N_{12}O_{60}Ir_4S_{12}Zn_4$: C, 12.73; H, 3.85; N, 4.95%. Found: C, 12.66; H, 3.67; N, 4.79%.

Anal. Calcd for $Sm_{0.33}[Sm_4(OH)_4(OAc)_3][\mathbf{1}^{Ir}]\cdot 22H_2O$ ($\mathbf{3}_{Sm}$) = $C_{42}H_{117}Sm_{4.33}N_{12}O_{57}Ir_4S_{12}Zn_4$: C, 13.39; H, 3.13; N, 4.46%. Found: C, 13.43; H, 3.27; N, 4.43%.

Anal. Calcd for $Eu_{0.33}[Eu_4(OH)_4(OAc)_3][\mathbf{1}^{Ir}]\cdot 21H_2O$ ($\mathbf{3}_{Eu}$) = $C_{42}H_{115}Eu_{4.33}N_{12}O_{56}Ir_4S_{12}Zn_4$: C, 13.42; H, 3.03; N, 4.47%. Found: C, 13.58; H, 3.18; N, 4.46%.

Anal. Calcd for $Gd_{0.33}[Gd_4(OH)_4(OAc)_3][\mathbf{1}^{Ir}]\cdot 28H_2O$ ($\mathbf{3}_{Gd}$) = $C_{42}H_{129}Gd_{4.33}N_{12}O_{63}Ir_4S_{12}Zn_4$: C, 12.91; H, 3.33; N, 4.30%. Found: C, 12.94; H, 3.35; N, 4.27%.

Anal. Calcd for $Tb_{0.33}[Tb_4(OH)_4(OAc)_3][\mathbf{1}^{Ir}]\cdot 32H_2O$ ($\mathbf{3}_{Tb}$) = $C_{42}H_{137}Tb_{4.33}N_{12}O_{67}Ir_4S_{12}Zn_4$: C, 12.66; H, 3.46; N, 4.22%. Found: C, 12.59; H, 3.33; N, 4.32%.

Anal. Calcd for $Dy_{0.33}[Dy_4(OH)_4(OAc)_3][\mathbf{1}^{Ir}]\cdot 21H_2O$ ($\mathbf{3}_{Dy}$) = $C_{42}H_{115}Dy_{4.33}N_{12}O_{56}Ir_4S_{12}Zn_4$: C, 13.26; H, 3.05; N, 4.42%. Found: C, 13.26; H, 3.11; N, 4.44%.

Anal. Calcd for $Ho_{0.33}[Ho_4(OH)_4(OAc)_3][\mathbf{1}^{Ir}]\cdot 23H_2O$ ($\mathbf{3}_{Ho}$) = $C_{42}H_{119}Ho_{4.33}N_{12}O_{58}Ir_4S_{12}Zn_4$: C, 13.10; H, 3.12; N, 4.37%. Found: C, 13.03; H, 3.10; N, 4.44%.

Anal. Calcd for $Er_{0.33}[Er_4(OH)_4(OAc)_3][\mathbf{1}^{Ir}]\cdot 29H_2O$ ($\mathbf{3}_{Er}$) = $C_{42}H_{131}Er_{4.33}N_{12}O_{64}Ir_4S_{12}Zn_4$: C, 12.71; H, 3.33; N, 4.24%. Found: C, 12.59; H, 3.24; N, 4.38%.

Anal. Calcd for $Tm_{0.33}[Tm_4(OH)_4(OAc)_3][\mathbf{1^{Ir}}]\cdot 25H_2O$ ($\mathbf{3_{Tm}}$) = $C_{42}H_{123}Tm_{4.33}N_{12}O_{60}Ir_4S_{12}Zn_4$: C, 12.92; H, 3.18; N, 4.31%. Found: C, 12.96; H, 3.21; N, 4.49%.

Anal. Calcd for $Yb_{0.33}[Yb_4(OH)_4(OAc)_3][\mathbf{1^{Ir}}]\cdot 25H_2O$ ($\mathbf{3_{Yb}}$) = $C_{42}H_{123}Yb_{4.33}N_{12}O_{60}Ir_4S_{12}Zn_4$: C, 12.86; H, 3.16; N, 4.29%. Found: C, 12.79; H, 3.16; N, 4.50%.

Anal. Calcd for $Lu_{0.33}[Lu_4(OH)_4(OAc)_3][\mathbf{1^{Ir}}]\cdot 24H_2O$ ($\mathbf{3_{Lu}}$) = $C_{42}H_{121}Lu_{4.33}N_{12}O_{59}Ir_4S_{12}Zn_4$: C, 12.90; H, 3.12; N, 4.30%. Found: C, 12.80; H, 3.10; N, 4.39%.

Physical measurements

The IR spectrum was recorded with a JASCO FT/IR-4100 infrared spectrophotometer using the ATR method at room temperature. Elemental analyses (C, H, N) were performed at Osaka University using a YANACO CHN Corder MT-5. X-ray fluorescence spectrometry was performed with a SHIMADZU EDX-7000 spectrometer. ^{1}H NMR spectra were recorded with a JEOL ECA500 (500 MHz) spectrometer in D_2O with sodium trimethylsilylpropanesulfonate (DSS) serving as an internal standard. High-quality powder X-ray diffraction (PXRD) was performed under ambient conditions in transmission mode (synchrotron radiation, λ= 0.8 Å; 2θ range = 2–78°; step width = 0.006°; data collection time = 1 min) on a diffractometer equipped with an MYTHEN microstrip X-ray detector (Dectris Ltd.) at the SPring-8 BL02B2 beamline.[31] The ground samples were placed in 0.3 mm glass capillary tubes with mother liquor. The samples were rotated during the measurements. The powder simulation patterns were generated from the single-crystal X-ray structures using Mercury 2023.2.[32] The absorption spectra in water were measured with a JASCO V-660 UV/VIS spectrometer at room temperature. The diffuse reflection spectra in the solid-state were measured with a JASCO V-670 UV/VIS spectrometer at room temperature using $MgSO_4$. The photoluminescence spectra were recorded with a JASCO FP-8500 spectrometer

at room temperature and 77 K. The internal emission quantum yield (Φ) was obtained via the absolute measuring method using an integrating sphere unit (JASCO ILFC-847); the internal surface was coated with highly reflective Spectralon. An ESC-842 calibrated light source (WI) and an ESC-843 calibrated light source (D2) were used to calibrate the emission intensities to measure the absolute quantum yields. The temperature-dependent magnetic susceptibility data were collected using a QUANTUM DESIGN MPMS XL7AC SQUID magnetometer under 0.1 T.

X-ray crystal structure determination.

The single-crystal X-ray diffraction dataset for $K_6[\mathbf{1^{Ir}}]\cdot n H_2O$ was collected at 200 K using a Rigaku FR-E Superbright rotating-anode X-ray source with a Mo target (λ = 0.71075 Å) equipped with a Rigaku RAXIS VII imaging plate as a detector. The datasets for $\mathbf{2_{Ln}}$ (Ln = La^{III}, Ce^{III}, Pr^{III}, Nd^{III}) and $\mathbf{3_{Ln}}$ (Ln = Eu^{III}, Gd^{III}, Tb^{III}, Ho^{III}, Tm^{III}, Yb^{III}, Lu^{III}), with the exception of $\mathbf{3_{Sm}}$, $\mathbf{3_{Dy}}$, and $\mathbf{3_{Er}}$, were collected at 100 K using a Synergy Custom X-ray diffractometer equipped with a Hypix-6000HE hybrid photon counting detector and a Rigaku VariMax rotating-anode X-ray source with a Mo target (λ = 0.71073 Å). The $\mathbf{3_{Sm}}$, $\mathbf{3_{Dy}}$, and $\mathbf{3_{Er}}$ datasets were collected using a PILATUS3 X CdTe 1M detector with a synchrotron X-ray source at the BL02B1 beamline at Spring-8. The intensity data were collected via the ω-scan technique and empirically corrected for absorption using Rigaku Rapid Auto or CrysAlicePro programs.[33,34] All structures were solved by the intrinsic phasing method within the SHELXT program [35] and were refined on F^2 by the full-matrix least-squares technique using the SHELXL program [36] via the Olex2 interface.[37]

The crystallographic data are summarized in Tables S1 and S2. All nonhydrogen atoms except for those in the disordered parts were refined anisotropically, while the other atoms were refined isotropically. The hydrogen atoms, with the exception of those on the water molecules, were

calculated and placed using riding models. Several RIGU and ISOR restraints were applied to regulate thermal ellipsoids, while DFIX, FLAT, and EADP were used to model the carboxylate groups. Most of the solvated water molecules could not be satisfactorily modeled and were, therefore, removed from the electron density map using the Olex2 solvent mask command. For $\mathbf{3_{Sm}}$ and $\mathbf{3_{Dy}}$, three OAc^- molecules in the cubane cluster could not be detected due to their high positional disorder.

Results and Discussion

Synthesis, characterization, and crystal structures of $K_6[\mathbf{1^{Ir}}]\cdot n H_2O$.

The starting $Ir^{III}_4Zn^{II}_4$ octanuclear complex, $(\Delta)_4$-$K_6[Zn_4O\{Ir(\text{L-cysteinate})_3\}_4]\cdot n H_2O$ ($K_6[\mathbf{1^{Ir}}]\cdot n H_2O$), was synthesized from Δ-$H_3[Ir(\text{L-cysteinate})_3]$, $ZnBr_2$, ZnO, and KOH in water according to a procedure similar to that used for $(\Delta)_4$-$K_6[Zn_4O\{Rh(\text{L-cysteinate})_3\}_4]\cdot n H_2O$ ($K_6[\mathbf{1^{Rh}}]\cdot n H_2O$);[38-40] however, Δ-$H_3[Ir(\text{L-cysteinate})_3]$ was used instead of Δ-$H_3[Rh(\text{L-cysteinate})_3]$. The results from X-ray fluorescence spectroscopy indicated that $K_6[\mathbf{1^{Ir}}]\cdot n H_2O$ contains Ir and Zn atoms in a 1:1 ratio, and its elemental analytical data agreed well with the expected formula for $K_6[\mathbf{1^{Ir}}]\cdot n H_2O$. The fully deprotonated state of the carboxylate groups of L-cysteinate in $K_6[\mathbf{1^{Ir}}]\cdot n H_2O$ was confirmed by the IR spectrum, which exhibited a strong C=O stretching band at 1586 cm^{-1} (Figure S1). In the ^1H NMR spectrum, $K_6[\mathbf{1^{Ir}}]\cdot n H_2O$ showed a single set of proton signals due to L-cysteinate (Figure S2), indicative of the highly symmetrical structure of $[\mathbf{1^{Ir}}]^{6-}$.

Single-crystal X-ray analysis showed that $K_6[\mathbf{1}^{\mathbf{Ir}}]\cdot n H_2O$ is isomorphous to $K_6[\mathbf{1}^{\mathbf{Rh}}]\cdot n H_2O$,[39] crystallized in the space group of cubic $P2_13$ (Table S1). As in the case of $K_6[\mathbf{1}^{\mathbf{Rh}}]\cdot n H_2O$, $K_6[\mathbf{1}^{\mathbf{Ir}}]\cdot n H_2O$ is composed of complex anions ($[\mathbf{1}^{\mathbf{Ir}}]^{6-}$) and K^+ cations in a 1:6 ratio, along with a number of water molecules of crystallization. As shown in Figure 1a, an O^{2-} ion is located at the center of the complex anion of $[\mathbf{1}^{\mathbf{Ir}}]^{6-}$, which is bound by four Zn^{II} atoms in a tetrahedral geometry to form a tetrahedral $[Zn_4O]^{6+}$ core. The four trigonal Zn^{II}_3 faces of the $[Zn_4O]^{6+}$ core in $[\mathbf{1}^{\mathbf{Ir}}]^{6-}$ are covered by three thiolato complexes from the Δ-[Ir(L-cysteinate)$_3$]$^{3-}$ unit, forming the *T* symmetrical $Ir^{III}_4Zn^{II}_4$ octanuclear structure in $[Zn_4O\{Ir(\text{L-cysteinate})_3\}_4]^{3-}$. This octanuclear structure is essentially the same as that in $[\mathbf{1}^{\mathbf{Rh}}]^{6-}$,[39] except for the presence of Δ-[Ir(L-cysteinate)$_3$]$^{3-}$ in place of Δ-[Rh(L-cysteinate)$_3$]$^{3-}$ in $[\mathbf{1}^{\mathbf{Rh}}]^{6-}$. The coordination bonds around Ir^{III} centers (av. Ir-S = 2.35 Å, av. Ir-N = 2.11 Å) in $K_6[\mathbf{1}^{\mathbf{Ir}}]\cdot n H_2O$ are slightly longer than those around Rh^{III} centers in $K_6[\mathbf{1}^{\mathbf{Rh}}]\cdot n H_2O$ (av. Rh-S = 2.34 Å, av. Rh-N = 2.10 Å), reflecting the larger ionic radius of Ir^{3+} (82 pm) compared with that of Rh^{3+} (80.5 pm).[41] In the crystal packing structure, each $[\mathbf{1}^{\mathbf{Ir}}]^{6-}$ anion is connected by six adjacent $[\mathbf{1}^{\mathbf{Ir}}]^{6-}$ anions through mutual NH···OOC hydrogen bonds (av. N···O = 2.84 Å), forming a 3D hydrogen-bonded framework (Figure 1b and 1c). This framework is also the same as that found in $K_6[\mathbf{1}^{\mathbf{Rh}}]\cdot n H_2O$, with the hydrogen-bonding distances similar to those in $K_6[\mathbf{1}^{\mathbf{Rh}}]\cdot n H_2O$ (av. N···O = 2.86 Å).[39] However, the total porosity of the hydrogen-bonded framework in $K_6[\mathbf{1}^{\mathbf{Ir}}]\cdot n H_2O$ (ca. 57%) is greater than that of the framework in $K_6[\mathbf{1}^{\mathbf{Rh}}]\cdot n H_2O$ (ca. 53%).

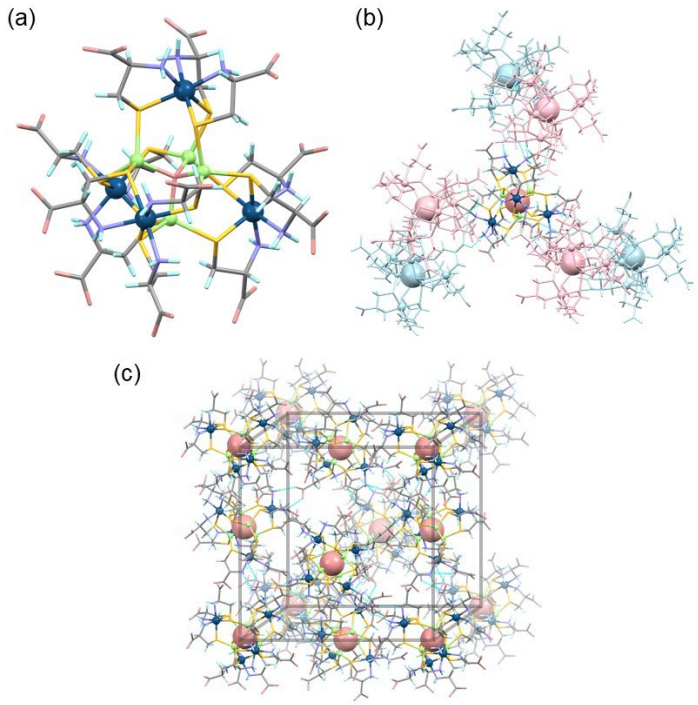

Figure 1. Perspective views of (a) the molecular structure of $[\mathbf{1}^{\mathbf{Ir}}]^{6-}$, (b) a complex anion surrounded by six adjacent complex anions (pale blue and pink), and (c) the 3D hydrogen-bonded framework in $K_6[\mathbf{1}^{\mathbf{Ir}}]\cdot n H_2O$. The central O atom of $[\mathbf{1}^{\mathbf{Ir}}]^{6-}$ was illustrated as the space-filling model for (b) and (c). Color code: Ir: dark cyan, Zn: yellow–green, S: yellow, O: pink, N: blue, C: gray, H: pale blue.

In crystal $K_6[\mathbf{1}^{\mathbf{Ir}}]\cdot n H_2O$, there exist two kinds of interstitial spaces: site A and site B, each of which is surrounded by three carboxylate groups from three different $[\mathbf{1}^{\mathbf{Ir}}]^{6-}$ anions. Each site accommodates a total of three K^+ ions through coordination bonds with the carboxylate groups; one K^+ ion is located at the center, and the other two K^+ ions are disordered at six positions around the central K^+ ion (Figure S3).[42] Notably, site B in $K_6[\mathbf{1}^{\mathbf{Ir}}]\cdot n H_2O$ is appreciably larger

than the corresponding site in $K_6[\mathbf{1}^{\mathbf{Rh}}]\cdot n H_2O$, although site A in $K_6[\mathbf{1}^{\mathbf{Ir}}]\cdot n H_2O$ is comparable in size to the corresponding site in $K_6[\mathbf{1}^{\mathbf{Rh}}]\cdot n H_2O$ (Figures S4a and S4b).

Synthesis, characterization, and crystal structures of $\mathbf{2_{Ln}}$ and $\mathbf{3_{Ln}}$.

To exchange K^I in $K_6[\mathbf{1}^{\mathbf{Ir}}]\cdot n H_2O$ with Ln^{III} (La^{III} – Lu^{III}), single crystals of $K_6[\mathbf{1}^{\mathbf{Ir}}]\cdot n H_2O$ were initially immersed in a 0.02 M ethanol-H_2O (3:1) mixture in a $Ln(OAc)_3$ solution due to their water solubility.[43] After a week of immersion, the crystals became insoluble in water, while their single crystallinity was retained. To complete the cation exchange reaction, the crystals were then immersed in a 0.1 M aqueous solution of $Ln(OAc)_3$ for 2 days, during which time the single crystallinity was also retained. The results from X-ray fluorescence spectroscopy indicated that each final product contains Ln atoms and lacked K atoms.[44] The retention of the molecular structure of $[\mathbf{1}^{\mathbf{Ir}}]^{6-}$ with Δ-[Ir(L-cysteinate)$_3$]$^{3-}$ units during the cation-exchange reaction was shown by the IR spectrum of each product, which was essentially the same as that of $K_6[\mathbf{1}^{\mathbf{Ir}}]\cdot n H_2O$ (Figure S1). Powder X-ray diffraction (PXRD) analysis revealed that the final products could be divided into two groups, $\mathbf{2_{Ln}}$ (Ln = La^{III}, Ce^{III}, Pr^{III}, and Nd^{III}) and $\mathbf{3_{Ln}}$ (Ln = Sm^{III}, Eu^{III}, Gd^{III}, Tb^{III}, Dy^{III}, Er^{III}, Ho^{III}, Tm^{III}, Yb^{III}, and Lu^{III}), based mainly on the relative diffraction intensities of the (111) and (200) indices (Figure S5). The structural differences between $\mathbf{2_{Ln}}$ and $\mathbf{3_{Ln}}$, as well as the isomorphism among $\mathbf{2_{La}}$, $\mathbf{2_{Ce}}$, $\mathbf{2_{Pr}}$, and $\mathbf{2_{Nd}}$ and among $\mathbf{3_{Sm}}$, $\mathbf{3_{Eu}}$, $\mathbf{3_{Gd}}$, $\mathbf{3_{Tb}}$, $\mathbf{3_{Dy}}$, $\mathbf{3_{Er}}$, $\mathbf{3_{Ho}}$, $\mathbf{3_{Tm}}$, $\mathbf{3_{Yb}}$, and $\mathbf{3_{Lu}}$, were determined by single-crystal X-ray crystallography (Tables S1 and S2).[45]

Compounds $\mathbf{2_{Ln}}$ (Ln = La^{III}, Ce^{III}, Pr^{III}, Nd^{III}) were all crystallized in the cubic space group of $P2_13$, and the representative crystal structure of $\mathbf{2_{La}}$ is described below. Crystal $\mathbf{2_{La}}$ contains $[\mathbf{1}^{\mathbf{Ir}}]^{6-}$ cluster anions and La^{III} cations in a 1:2 ratio, in addition to a number of water molecules; this forms an ionic crystal of $La_2[\mathbf{1}^{\mathbf{Ir}}]\cdot n H_2O$. Not only the molecular structure of $[\mathbf{1}^{\mathbf{Ir}}]^{6-}$ but also

the 3D framework structure of $\mathbf{2_{La}}$, in which $[\mathbf{1^{Ir}}]^{6-}$ anions are hydrogen-bonded to each other (av. N···O = 2.84 Å), is nearly the same as that in $K_6[\mathbf{1^{Ir}}]\cdot n H_2O$, with two kinds of triangular spaces corresponding to site A and site B in $K_6[\mathbf{1^{Rh}}]\cdot n H_2O$ (Figure S6). The cationic species of La^{III} are disordered into five crystallographically independent positions with occupancy factors of 0.20 for La1A, 0.0833 for La1B, 0.05 for La1C, 0.25 for La2A, and 0.0833 for La2B. As shown in Figure 2, La1B and La1C atoms exist at the center of site B and are surrounded by three La1A atoms that are coordinated by the carboxylate groups from $[\mathbf{1^{Ir}}]^{6-}$ anions. On the other hand, three La2B atoms exist at site A and are coordinated by carboxylate groups from $[\mathbf{1^{Ir}}]^{6-}$anions. To balance the charge of the crystal $\mathbf{2_{La}}$ with the formula $La_2[\mathbf{1^{Ir}}]\cdot n H_2O$, the La2A atoms exist outside site A, bound by the carboxylate groups from $[\mathbf{1^{Ir}}]^{6-}$ anions (Figure 2). The overall distribution of the Ln^{III} ions in $\mathbf{2_{Ln}}$ resembles that of the K^+ ions in $K_6[\mathbf{1^{Ir}}]\cdot n H_2O$ (Figures S3 and S7a). This reflects the PXRD profile of $\mathbf{2_{Ln}}$, which is very similar to that of $K_6[\mathbf{1^{Ir}}]\cdot n H_2O$ (Figure S5).

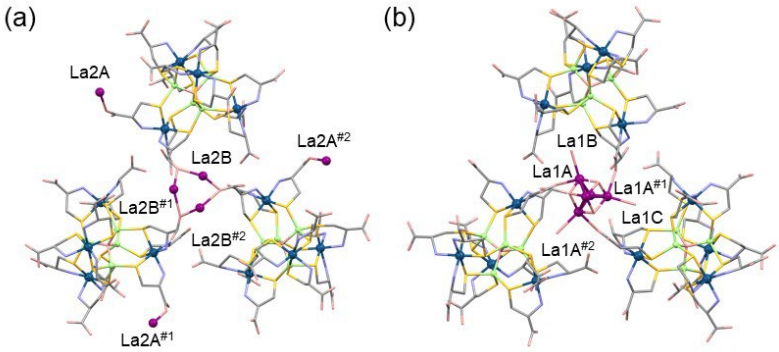

Figure 2. Perspective view of $\mathbf{2_{La}}$: (a) site A and (b) site B accommodating La^{III} ions. Color code: Ir: dark cyan, Zn: yellow–green, La: deep purple, S: yellow, O: pink, N: blue, C: gray. Symmetry code: #1: 3/2-z, 1-x, 1/2+y; #2: 1-y, -1/2+z, 3/2-x.

As in the case of $\mathbf{2_{Ln}}$ (Ln = La^{III}, Ce^{III}, Pr^{III}, Nd^{III}), all compounds of $\mathbf{3_{Ln}}$ (Ln = Sm^{III}, Eu^{III}, Gd^{III}, Tb^{III}, Dy^{III}, Er^{III}, Ho^{III}, Tm^{III}, Yb^{III}, Lu^{III}) crystallized in the cubic space group of $P2_13$. In addition, the $[\mathbf{1^{Ir}}]^{6-}$ anions in $\mathbf{3_{Ln}}$ formed a 3D hydrogen-bonded framework that is essentially the same as the framework in $K_6[\mathbf{1^{Ir}}]\cdot n H_2O$ (Figures S8 and S9). However, the Ln^{III} ions in $\mathbf{3_{Ln}}$ existed in a cubane form at site B rather than in a discrete form. Figure 3 shows the structure of $\mathbf{3_{Lu}}$ as a representative of $\mathbf{3_{Ln}}$. At site B, four Lu^{III} atoms (Lu1 and Lu2) are bridged by four μ_3-OH^- ions to form a $[Lu_4(OH)_4]^{8+}$ cubane core with an average Lu-O bond distance and Lu···Lu distance of 2.31 Å and 3.67 Å, respectively (Figure 3a and 3c). The assignment of the μ_3-bridging species as OH^-, rather than O^{2-} or H_2O, was based on the average Lu–O bond distance, which is within the range normally observed for the Lu^{III}-OH^- bonds in $[Lu_4(OH)_4]^{8+}$,[29,46] together with the charge balance of the crystal. The $[Lu_4(OH)_4]^{8+}$ cubane core is bound by three OAc^- ions, each of which spans two Ln^{III} centers through its carboxylate group (av. Lu-O = 2.24 Å). In addition, a total of seven water molecules coordinate to the Ln^{III} centers (av. Lu-O = 2.34 Å), completing the cubane structure in $[Lu_4(OH)_4(OAc)_3(H_2O)_7]^{5+}$ (Figure 3a). The vacant coordination sites of the Ln^{III} centers in $[Lu_4(OH)_4(OAc)_3(H_2O)_7]^{5+}$ are occupied by three carboxylate groups from three $[\mathbf{1^{Ir}}]^{6-}$ anions (av. Lu-O = 2.30 Å); this leads to the formation of a 3D coordination polymer composed of $[Lu_4(OH)_4(OAc)_3(H_2O)_7]^{5+}$ cations and [$\mathbf{1^{Ir}}$[$^{6-}$ anions in $\mathbf{3_{Lu}}$ (Figures 3c and S8j). To balance the charge of the crystal with a chemical formula of $Lu_{0.33}[Lu_4(OH)_4(OAc)_3(H_2O)_7]]\mathbf{1^{Ir}}]\cdot n H_2O$, $\mathbf{3_{Lu}}$ contains a disordered Lu^{III} (Lu3) ion with an occupancy of 0.0311 at site A and a discrete aqua Lu^{III} (Lu4) ion with an occupancy of 0.08 at a triangular space other than site A and site B (Figures 3b and 3d).

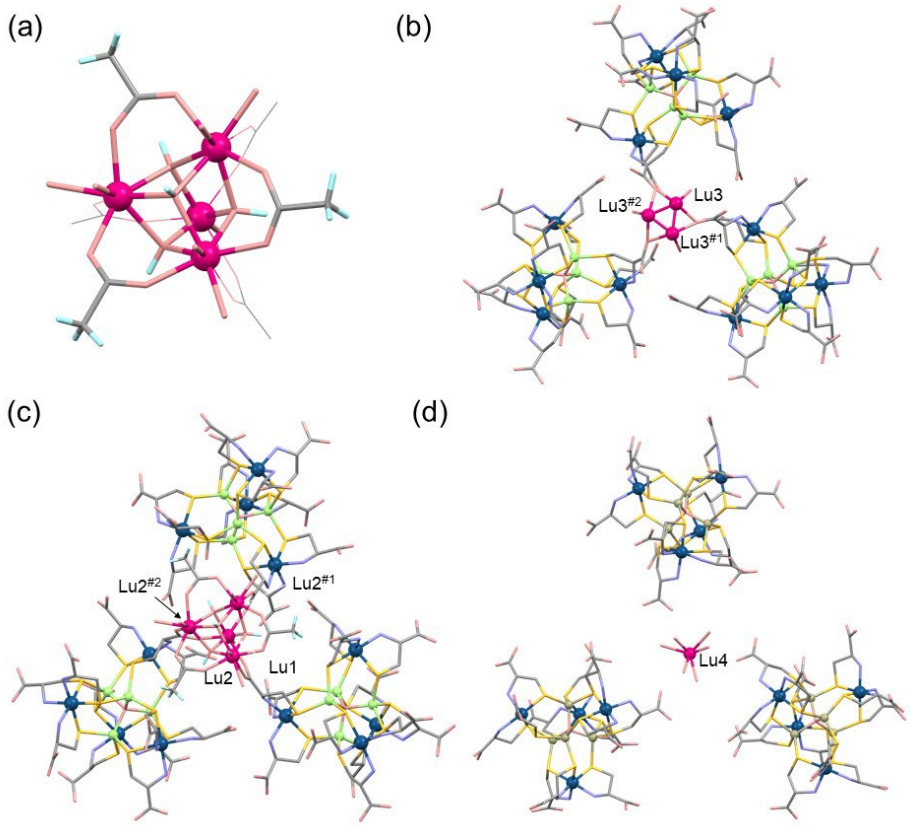

Figure 3. Perspective views of **3**$_{\mathbf{Lu}}$ (a) $[Lu_4(OH)_4(OAc)_3(H_2O)_7]^{5+}$ cubane cluster, (b) site A accommodating a disordered Lu^{III} ion, (c) site B accommodating the cubane cluster, and (d) a triangular space accommodating an aqua Lu^{III} ion. Color code: Ir: dark cyan, Zn: yellow–green, Lu: red–purple, S: yellow, O: pink, N: blue, C: gray. Symmetry code: #1: 1+z, x, -1+y; #2: y, 1+z, -1+x.

The cubane structures of $[Ln_4(OH)_4(OAc)_3(H_2O)_7]^{5+}$ in **3**$_{\mathbf{Ln}}$ (Ln = Sm^{III}, Eu^{III}, Gd^{III}, Tb^{III}, Dy^{III}, Er^{III}, Ho^{III}, Tm^{III}, Yb^{III}, Lu^{III}) are nearly the same as each other (Figures 3a and 4). However, the Ln····Ln distances in the cubanes gradually decrease from **3**$_{\mathbf{Sm}}$ (3.87 Å) to **3**$_{\mathbf{Lu}}$ (3.67 Å); this result is consistent with the decrease in Ln^{3+} ionic radii in the lanthanide series (Table

S3).[25] Here, the 3D polymeric structure in $Ln_{0.33}[Ln_4(OH)_4(OAc)_3(H_2O)_7][\mathbf{1^{Rh}}]$, which is analogous to that in $\mathbf{3_{Ln}}$, was formed for a lanthanide series later than Gd^{III}, while a lanthanide series earlier than Eu^{III} produced ionic crystals of $Ln_2[\mathbf{1^{Rh}}]$ analogous to $\mathbf{2_{Ln}}$.[29] Thus, the use of $K_6[\mathbf{1^{Ir}}]$ as the starting compound, instead of $K_6[\mathbf{1^{Rh}}]$, led to the expansion of the lanthanide series that forms $[Ln_4(OH)_4]^{8+}$ cubanes in the framework, with the addition of Sm^{III} and Eu^{III} to the Gd^{III} - Lu^{III} series. Since no significant difference was observed in cubane size between $\mathbf{3_{Ln}}$ and $Ln_{0.33}[Ln_4(OH)_4(OAc)_3(H_2O)_7][\mathbf{1^{Rh}}]$ (Table S3), the expansion of the lanthanide series for $\mathbf{3_{Ln}}$ is ascribed to the formation of the triangular space of site B in $K_6[\mathbf{1^{Ir}}]\cdot n H_2O$, which is larger than the corresponding space in $K_6[\mathbf{1^{Rh}}]\cdot n H_2O$.

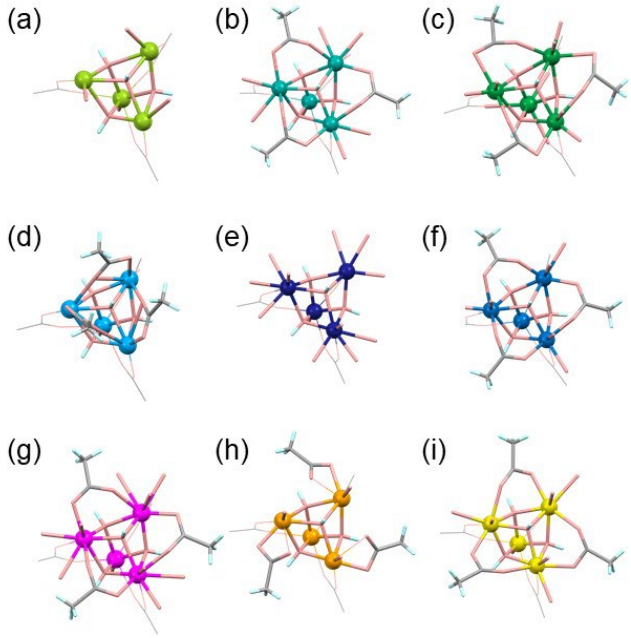

Figure 4. Perspective views of $[Ln_4(OH)_4(OAc)_3(H_2O)_7]^{5+}$ clusters in (a) $\mathbf{3_{Sm}}$, (b) $\mathbf{3_{Eu}}$, (c) $\mathbf{3_{Gd}}$, (d) $\mathbf{3_{Tb}}$, (e) $\mathbf{3_{Dy}}$, (f) $\mathbf{3_{Ho}}$, (g) $\mathbf{3_{Er}}$, (h) $\mathbf{3_{Tm}}$, and (i) $\mathbf{3_{Yb}}$.

Magnetic properties.

The temperature-dependent magnetic susceptibilities of a series of solid samples of $\mathbf{2}_{\mathbf{Ln}}$ and $\mathbf{3}_{\mathbf{Ln}}$, with the exception of $\mathbf{2}_{\mathbf{La}}$ and $\mathbf{3}_{\mathbf{Lu}}$ that are diamagnetic, were measured in the temperature range of 2–300 K at an applied magnetic field of 1000 Oe. As shown in Figure 5a, the observed plots of $\chi_m T$ vs. T for $\mathbf{2}_{\mathbf{Ce}}$, $\mathbf{2}_{\mathbf{Pr}}$, and $\mathbf{2}_{\mathbf{Nd}}$ show a gradual decrease in $\chi_m T$ with decreasing temperature due to the decrease in the thermal population of the m_j microstate of Ln^{3+}.[47] At 300 K, the observed $\chi_m T$ values (cm^3Kmol^{-1}) for $\mathbf{2}_{\mathbf{Ce}}$ (1.49), $\mathbf{2}_{\mathbf{Pr}}$ (3.49), and $\mathbf{2}_{\mathbf{Nd}}$ (3.98) are similar to Van Vleck's theoretical values for the two discrete ions Ce^{3+} (1.64), Pr^{3+} (3.20), and Nd^{3+} (3.39), respectively.[47,48] This is also the case for $\mathbf{3}_{\mathbf{Ln}}$ (Figure 5b); the observed $\chi_m T$ values (cm^3Kmol^{-1}) for $\mathbf{3}_{\mathbf{Sm}}$ (1.25), $\mathbf{3}_{\mathbf{Eu}}$ (6.44), $\mathbf{3}_{\mathbf{Gd}}$ (32.4), $\mathbf{3}_{\mathbf{Tb}}$ (42.1), $\mathbf{3}_{\mathbf{Dy}}$ (53.5), $\mathbf{3}_{\mathbf{Ho}}$ (53.6), $\mathbf{3}_{\mathbf{Er}}$ (43.5), $\mathbf{3}_{\mathbf{Tm}}$ (24.3), and $\mathbf{3}_{\mathbf{Yb}}$ (9.63) at 300 K are similar to the theoretical $\chi_m T$ values for the 4.33 discrete ions Sm^{3+} (1.30), Eu^{3+} (6.25), Gd^{3+} (34.1), Tb^{3+} (51.0), Dy^{3+} (61.1), Ho^{3+} (60.8), Er^{3+} (49.9), Tm^{3+} (31.3), and Yb^{3+} (10.9), respectively.[47,48] As the representative compound, the magnetic susceptibility data of $\mathbf{3}_{\mathbf{Gd}}$ that contains magnetically isotropic Gd^{III} centers were fitted using a PHI program,[49] based on the following Hamiltonian where the first and second terms are the isotropic exchange interaction and the Zeeman term of four Gd^{III} ions in the cubane structure at site B, respectively, and the third term is the isolated Gd^{III} ion at site A:

$$H = -2J\left(\hat{S}_1\hat{S}_2 + \hat{S}_1\hat{S}_3 + \hat{S}_1\hat{S}_4 + \hat{S}_2\hat{S}_3 + \hat{S}_2\hat{S}_4 + \hat{S}_3\hat{S}_4\right) + g\mu_B H\sum_{i=1}^{4} S_i + \frac{1}{3}g\mu_B H S_5 + T.I.P.$$

The fitting of the experimental curve indicated the presence of very weak anti-ferromagnetic interactions of J = –0.0184(1) cm^{-1} among Gd^{III} ions (Figure S10). This $|J|$ value for $\mathbf{3}_{\mathbf{Gd}}$ is much smaller than the values (–0.03 ~ –0.08 cm^{-1}) for previously reported $[Gd_4O_4]$-type clusters that commonly adopt a C_1 symmetry.[8,19,50-52] We assumed that the high-symmetrical cubane structure, as well as the location of the cubanes that are largely separated from each other through $[\mathbf{1}^{\mathbf{Ir}}]^{6-}$

complex anions (Figure S8), is responsible for the negligibly small magnetic interactions among the Gd^{III} centers in $\mathbf{3_{Gd}}$. While the simulations for $\mathbf{3_{Ln}}$ that contain magnetically anisotropic Ln^{III} ions could not be performed, the absence of any significant magnetic interactions between Ln^{III} centers is also expected for $\mathbf{3_{Ln}}$, considering the isostructural nature of a series of $\mathbf{3_{Ln}}$.

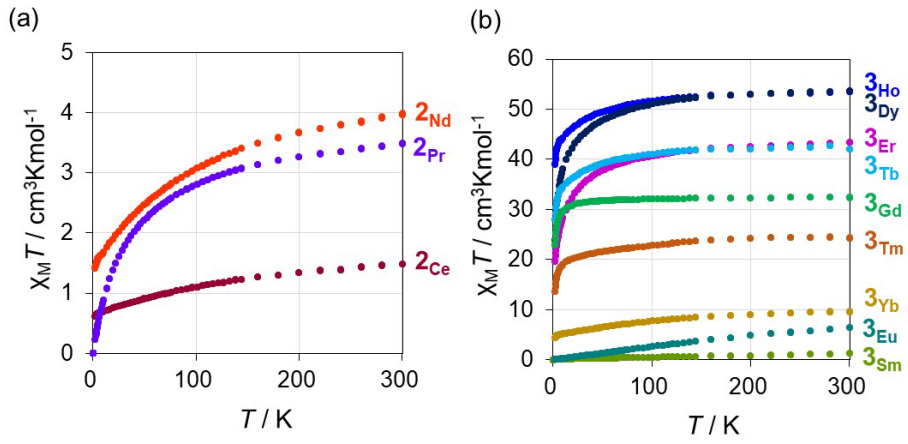

Figure 5. $\chi_M T$ vs. T plots of (a) $\mathbf{2_{Ln}}$ and (b) $\mathbf{3_{Ln}}$ (H = 1000 Oe).

Photoluminescent properties

At 77 K, a solid sample of $K_6[\mathbf{1^{Ir}}]$ exhibits a broad emission band at 610 nm with a quantum efficiency of 4.4% under excitation at 370 nm (Figure S11), while no emission was detected at room temperature due to thermal vibration at a high temperature. Since a similar broad emission band was observed for a bulk sample of zinc oxide, the emission band is attributed to the O-to-Zn charge transfer transition in the $[Zn_4O]^{6+}$ core.[53-56] However, the emission band for $K_6[\mathbf{1^{Ir}}]$ was located at a lower energy than the band for zinc oxide at 510 nm (Figure S11). The redshift of the emission band for $K_6[\mathbf{1^{Ir}}]$ is most likely due to the larger vibrational perturbation of its hydrogen-bonded framework compared with the rigid framework of zinc oxide, which results in a greater

Stokes shift than that for zinc oxide.[57] Notably, $K_6[\mathbf{1}^{\mathbf{Rh}}]$ is nonemissive even at 77 K because $K_6[\mathbf{1}^{\mathbf{Rh}}]$ possesses d-d transition bands centered at 324 nm and 370 nm tailing to the visible region (Figure S12), which overlaps the charge transfer bands arising from the $[Zn_4O]^{6+}$ core. Thus, irradiation with excitation light caused unfavorable energy transfer to the nonemissive d-d excited states of the Rh^{III} center rather than luminescence from the radiative excited states of the $[Zn_4O]^{6+}$ core. On the other hand, $K_6[\mathbf{1}^{\mathbf{Ir}}]$ has corresponding d-d bands at 240 nm and 278 nm with no significant absorption in the visible region (Figure S12), which allows $K_6[\mathbf{1}^{\mathbf{Ir}}]$ to be photoluminescent.[58]

Since $K_6[\mathbf{1}^{\mathbf{Ir}}]$ was found to be emissive, we investigated the photoluminescence properties of solid samples of $\mathbf{3}_{\mathbf{Eu}}$ and $\mathbf{3}_{\mathbf{Tb}}$, considering that Eu^{III} and Tb^{III} species are strongly luminescent.[25] As shown in Figures 6a and 6b, sharp emission bands are observed for $\mathbf{3}_{\mathbf{Eu}}$ and $\mathbf{3}_{\mathbf{Tb}}$ at room temperature, with quantum efficiencies of 0.22% and 0.21% under excitation at 395 nm and 370 nm, respectively; these results reflect the high rigidity of the coordination framework of these compounds. The emission spectral features of $\mathbf{3}_{\mathbf{Eu}}$ and $\mathbf{3}_{\mathbf{Tb}}$ are characteristic of the *f-f* transitions $^5D_0 \rightarrow {}^7F_J$ (J = 1–4) and $^5D_4 \rightarrow {}^7F_J$ (J = 6–3); these are commonly observed for discrete Eu^{III} and Tb^{III} species, respectively.[25] This observation is compatible with the absence of any significant magnetic interactions between Ln^{III} centers in $\mathbf{3}_{\mathbf{Ln}}$. At 77 K, $\mathbf{3}_{\mathbf{Eu}}$ and $\mathbf{3}_{\mathbf{Tb}}$ each exhibit a broad emission band at approximately 625 nm with quantum efficiencies of 3.6% and 4.0%, respectively, which originated from the $[\mathbf{1}^{\mathbf{Ir}}]^{6-}$ units in these compounds, in addition to the sharp *f-f* transition bands that are essentially the same as the bands observed at room temperature (Figures 6c and 6d). The simultaneous observation of the two kinds of emissions for $\mathbf{3}_{\mathbf{Eu}}/\mathbf{3}_{\mathbf{Tb}}$ is understood by the negligible overlap between the absorption bands due to $[\mathbf{1}^{\mathbf{Ir}}]^{6-}$ units and the excitation bands due to Eu^{III}/Tb^{III} centers (λ_{ex} = 395 nm for Eu^{III}, λ_{ex} = 370 nm for Tb^{III}), preventing energy transfer

from [$\mathbf{1}^{\mathbf{Ir}}$]$^{6-}$ units to Eu^{III}/Tb^{III} centers in $\mathbf{3}_{\mathbf{Eu}}$/$\mathbf{3}_{\mathbf{Tb}}$. Unlike for $\mathbf{3}_{\mathbf{Eu}}$/$\mathbf{3}_{\mathbf{Tb}}$, characteristic *f-f* emissions were not detected for the corresponding compounds with [$\mathbf{1}^{\mathbf{Rh}}$]$^{6-}$ units of $Ln_{0.33}[Ln_4(OH)_4(OAc)_3(H_2O)_7][\mathbf{1}^{\mathbf{Rh}}]$ (Ln = Eu^{III}, Tb^{III}) because of the presence of the d-d absorptions in the visible region. Notably, the excitation spectra of $\mathbf{3}_{\mathbf{Eu}}$/$\mathbf{3}_{\mathbf{Tb}}$ differ entirely from the absorption spectra of $\mathbf{3}_{\mathbf{Eu}}$/$\mathbf{3}_{\mathbf{Tb}}$ (Figure S13), showing the characteristic f-f transitions due to Eu^{III}/Tb^{III} centers.[25,59,60] In general, the *f-f* emissions for lanthanide(III) coordination compounds are induced by photoenergy that is absorbed by ligands bound to Ln^{III} centers; thus, the excitation spectra of these compounds resemble their absorption spectra.[25,61] In $\mathbf{3}_{\mathbf{Eu}}$/$\mathbf{3}_{\mathbf{Tb}}$, luminescence occurs based on the photoenergy directly absorbed by Eu^{III}/Tb^{III} centers because of the lack of ligand-to-Ln^{III} energy transfer, leading to unique excitation spectral features for $\mathbf{3}_{\mathbf{Eu}}$/$\mathbf{3}_{\mathbf{Tb}}$.

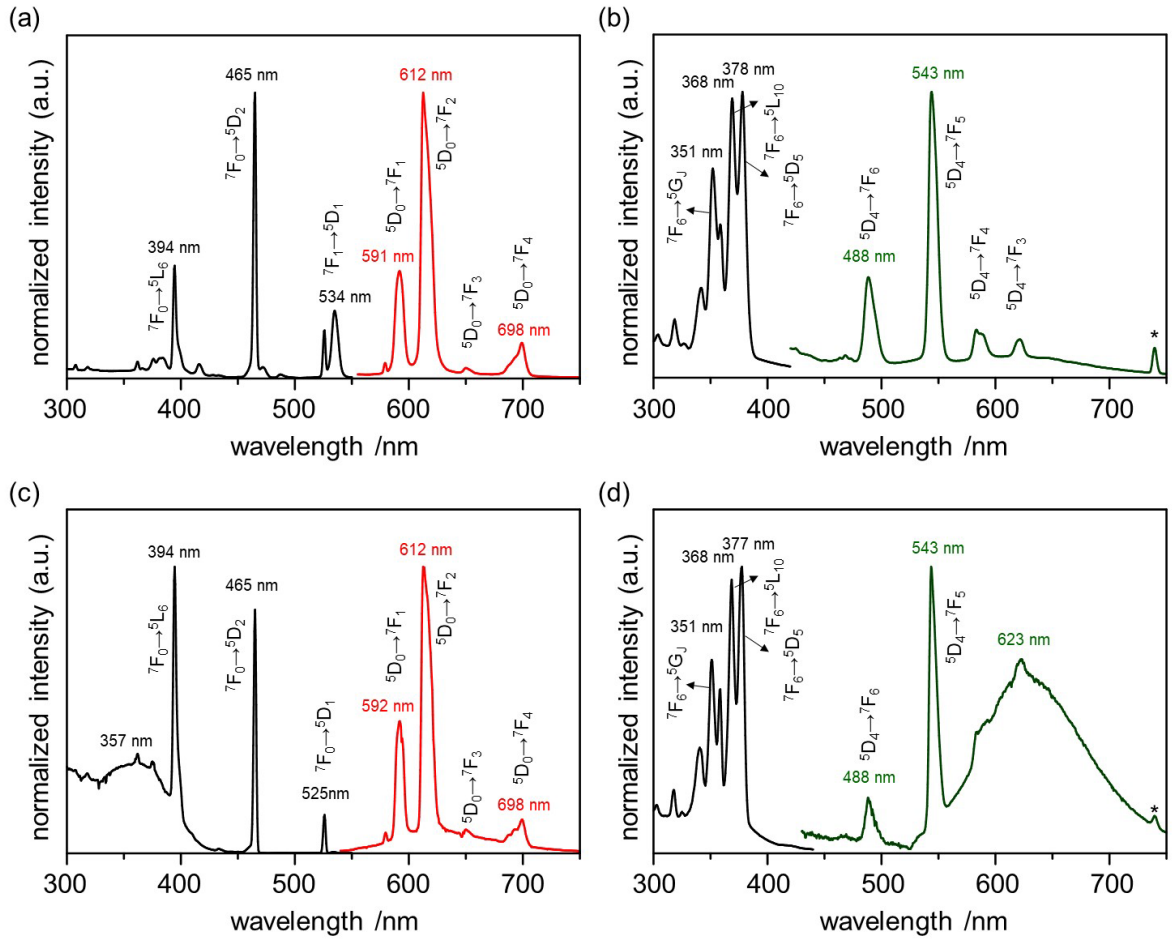

Figure 6. Excitation (black, λ_{em} = 615 nm) and emission (red, λ_{ex} = 395 nm) spectra of $\mathbf{3}_{\mathbf{Eu}}$ (a) at room temperature and (c) at 77 K. Excitation (black, λ_{em} = 546 nm) and emission (red, λ_{ex} = 370 nm) spectra of $\mathbf{3}_{\mathbf{Tb}}$ (b) at room temperature and (d) at 77 K.

Concluding Remarks

We showed that K^{I} ions in $K_6[\mathbf{1}^{\mathbf{Ir}}]\cdot n H_2O$ newly prepared in this work are completely exchanged with Ln^{III} ions in an SCSC transformation manner to produce $\mathbf{2}_{\mathbf{Ln}}$ and $\mathbf{3}_{\mathbf{Ln}}$, by immersing its crystals in an aqueous solution of $Ln(OAc)_3$. While similar results have been obtained when $K_6[\mathbf{1}^{\mathbf{Rh}}]\cdot n H_2O$

was used for the cation exchange reaction with Ln^{III}, the use of $K_6[\mathbf{1}^{\mathbf{Ir}}]\cdot n H_2O$ allowed the installation of $Ln_4(OH)_4$ cubanes to form $\mathbf{3_{Ln}}$ for the lanthanide series later than Sm^{III}. Since the installation of lanthanide ions in the $Ln_4(OH)_4$ cubane form was observed for the lanthanide series later than Gd^{III} for the cation exchange reactions for $K_6[\mathbf{1}^{\mathbf{Rh}}]\cdot n H_2O$, the replacement of Rh^{III} centers in $[\mathbf{1}^{\mathbf{Rh}}]^{6-}$ by the heavier congener of Ir^{III} led to the expansion of the series of $Ln_4(OH)_4$ cubanes created via the SCSC cation exchange reactions. This is thanks to the larger interstices formed in the hydrogen-bonded framework of $[\mathbf{1}^{\mathbf{Ir}}]^{6-}$, which can accommodate $Ln_4(OH)_4$ cubanes with larger Ln^{III} ions. In $\mathbf{3_{Ln}}$, the $Ln_4(OH)_4$ cubanes were alternately connected by the large complex anions of $[\mathbf{1}^{\mathbf{Ir}}]^{6-}$ such that the cubanes are fully separated from each other. This structural feature, together with the symmetry of the four Ln^{III} centers in $Ln_4(OH)_4$, accounts for the magnetic susceptivity curves of $\mathbf{3_{Ln}}$, which are essentially the same as those of the isolated Ln^{III} species.

In addition to the expansion of the series of $Ln_4(OH)_4$ cubanes, the replacement of Rh^{III} by Ir^{III} led this system to be photoluminescent because of the shift of d-d transitions in $[\mathbf{1}^{\mathbf{Rh}}]^{6-}$ to the near-UV energy region in $[\mathbf{1}^{\mathbf{Ir}}]^{6-}$. Notably, the sharp emission bands due to Ln^{III} centers, which overlapped the broad band due to the $[Zn_4O]^{6+}$ core, were observed for $\mathbf{3_{Eu}}$ and $\mathbf{3_{Tb}}$ at low temperatures. Furthermore, $\mathbf{3_{Eu}}$ and $\mathbf{3_{Tb}}$ exhibited sharp excitation bands that are characteristically observed for discrete Eu^{III}/Tb^{III} species, rather than broad excitation bands that resemble their absorption bands. These observations indicate that no energy transfer occurs from the $[\mathbf{1}^{\mathbf{Ir}}]^{6-}$ units to the $Ln_4(OH)_4$ core through the coordination bonds in $\mathbf{3_{Ln}}$; this phenomenon is rare for coordination systems with Ln^{III} centers. The photoluminescence ability of this system can be enhanced by the replacement of the acetate ligands bound to the $Ln_4(OH)_4$ core in $\mathbf{3_{Ln}}$ by suitable antenna ligands; these can cause effective intramolecular energy transfer from ligands to Ln^{III} centers. This research is currently being performed in our laboratory.

ASSOCIATED CONTENT

Data Availability Statement

The data underlying this study are available in the published article and its supporting information.

Supporting Information.

The Supporting Information is available free of charge. Experimental information, spectroscopic data, magnetic resonance data, and X-ray crystal structure data (PDF).

Accession Codes

CCDC 2312730-2312744 contain the supplementary crystallographic data for this paper. These data can be obtained free of charge via www.ccdc.cam.ac.uk/data_request/cif, by emailing data_request@ccdc.cam.ac.uk, or by contacting the Cambridge Crystallographic Data Centre, 12 Union Road, Cambridge CB2 1EZ, UK; fax: +44 1223 336033.

AUTHOR INFORMATION

Corresponding Author

*Nobuto Yoshinari

Email: nobuto@chem.sci.osaka-u.ac.jp

*Takumi Konno

Email: konno@chem.sci.osaka-u.ac.jp

Author Contributions

ST and TM performed the syntheses and characterization of the compounds; ST and AR performed the spectroscopic measurements; NY performed the X-ray diffraction analysis and magnetic measurements; ST, NY, and TK prepared the manuscript; and NY and TK conceived the project. All authors have approved the final version of the manuscript.

Notes

The authors declare no competing financial interest.

ACKNOWLEDGMENT

This work was supported by JSPS KAKENHI (Grant No. 19K05496). The synchrotron radiation experiments were performed at the BL02B1 and BL02B2 beamlines of SPring-8 with the approval of the Japan Synchrotron Radiation Research Institute (JASRI) (Proposal Nos. 2020A1551, 2021B1354, 2021B1475, 2022A1573, 2022B1806, and 2022B1659).

REFERENCES

1. Woodruff, D. N.; Winpenny, R. E.; Layfield, R. A. Lanthanide Single-Molecule Magnets. *Chem. Rev.* **2013**, *113*, 5110-5148.

2. Brunet, G.; Hamwi, M.; Lemes, M. A.; Gabidullin, B.; Murugesu, M. A tunable lanthanide cubane platform incorporating air-stable radical ligands for enhanced magnetic communication *Commun. Chem.* **2018**, *1*, 88.

3. Qin, L.; Yu, Y.-Z.; Liao, P.-Q.; Xue, W.; Zheng, Z.; Chen, X.-M.; Zheng, Y.-Z. A "Molecular Water Pipe": A Giant Tubular Cluster {Dy_{72}} Exhibits Fast Proton Transport and Slow Magnetic Relaxation. *Adv. Mater.* **2016**, *28*, 10772-10779.

4. Zheng, X. Y.; Xie, J.; Kong, X. J.; Long, L. S.; Zheng, L. S. Recent advances in the assembly of high-nuclearity lanthanide clusters. *Coord. Chem. Rev*. **2019**, *378*, 222–236.

5. Wang, R.; Selby, H. D.; Liu, H.; Carducci, M. D.; Jin, T.; Zheng, Z.; Anthis, J. W.; Staples, R. J. Halide-Templated Assembly of Polynuclear Lanthanide-Hydroxo Complexes. *Inorg. Chem*. **2002**, *41*, 278-286.

6. Zheng, Z. Ligand-controlled self-assembly of polynuclear lanthanide–oxo/hydroxo complexes: from synthetic serendipity to rational supramolecular design. *Chem. Commun*. **2001**, 2521-2529.

7. Singh-Wilmot, M. A.; Kahwa, I. A.; White, A. J. P.; Williams, D. J.; Lough, A. J. Tunable electronic interactions in small lanthanide(III) nanoclusters: The comparative effects of OH^- and O^{2-} supramolecular glues on europium(III)-to-dysprosium(III) energy transfer. *Polyhedron* **2010**, *29*, 270-279.

8. Litvinova, Y. M.; Gayfulin, Y.M.; Leusen, J. V.; Samsonenko, D. G.; Lazarenko, V. A.; Zubavichus, Y. V.; Kögerler, P.; Mironov, Y. V. Metal–organic frameworks based on polynuclear lanthanide complexes and octahedral rhenium clusters. *Inorg. Chem. Front.* **2019**, *6*, 1518-1526.

9. Wong, H. Y.; Chan, W. T. K.; Law, G. L. Assembly of Lanthanide(III) Cubanes and Dimers with Single-Molecule Magnetism and Photoluminescence. *Inorg. Chem.* **2018**, 57, 6893-6902.

10. Zhang, H.-Y.; Yu, H.-J.; Xu, H.-X.; Ren, J.-S.; Qu, X.-G. Structural diversity of lanthanide–amino acid complexes under near physiological pH conditions and their recognition of single-stranded DNA. *Polyhedron* **2007**, *26*, 5250-5256.

11. Ma, B.-Q.; Zhang, D.-S.; Gao, S.; Jin, T.-Z.; Yan, C.-H; Xu, G.-X. From Cubane to Supercubane: The Design,Synthesis, and Structure of a Three-Dimensional Open Framework Based on a Ln_4O_4 Cluster. *Angew. Chem. Int. Ed.* **2000**, *39*, 3515-3710.

12. Ma, B.-Q.; Zhang, D.-S.; Gao, S.; Jin, T.-Z.; Yan, C.-H. The formation of Gd_4O_4 cubane cluster controlled by L-valine. *New J. Chem.* **2000**, *24*, 251-252.

13. Wang, R.; Liu, H.; Carducci, M. D.; Jin, T.; Zheng, C.; Zheng, Z. Lanthanide Coordination with α-Amino Acids under Near Physiological pH Conditions: Polymetallic Complexes Containing the Cubane-Like $[Ln_4(\mu_3\text{-}OH)_4]^{8+}$ Cluster Core. *Inorg. Chem.* **2001**, *40*, 2743-2750.

14. Gerasko, O. A.; Mainicheva, E. A.; Naumova, M. I.; Neumaier, M.; Kappes, M. M.; Lebedkin, S.; Fenske, D.; Fedin, V. P. Sandwich-Type Tetranuclear Lanthanide Complexes with Cucurbit[6]uril: From Molecular Compounds to Coordination Polymers. *Inorg. Chem.* **2008**, *47*, 8869-8880.

15. Kong, X.-J.; Long, L.-S.; Zheng, L.-S.; Wang, R.; Zheng, Z. Hydrolytic Synthesis and Structural Characterization of Lanthanide Hydroxide Clusters Supported by Nicotinic Acid. *Inorg. Chem.* **2009**, *48*, 3268-3273.

16. Li, X.; Wua, X.-S.; Zheng, X.-J. A 2-D polymer assembled by cubane-like clusters $[Tb_4(OH)_4(phen)_3(H_2O)_3]^{8+}$ and 3-sulfobenzoate. *Inorg. Chim. Acta* **2009**, *362*, 2537-2541.

17. Savard, D.; Lin, P.-H.; Burchell, T. J.; Korobkov, I.; Wernsdorfer, W.; Clérac, R.; Murugesu, M. Two-Dimensional Networks of Lanthanide Cubane-Shaped Dumbbells. *Inorg. Chem.* **2009**, *48*, 11748-11754.

18. Yi, X.; Bernot, K.; Calvez, G.; Daiguebonne, C.; Guillou, O. 3D Organization of Dysprosium Cubanes. *Eur. J. Inorg. Chem.* **2013**, 5879-5885.

19. Xiong, G.; You, L.; Ren, B.; He, Y.; Wang, S.; Sun, Y. Structure and Magnetocaloric Effect of Two Kinds of Ln–Mn^{II} Heterometallic Coordination Polymers Produced by Fractional Crystallization. *Eur. J. Inorg. Chem.* **2016**, 3969-3977.

20. Wu, H.; Zhang, S.; Li, M.; Qiao, C.; Sun, L.; Wei, Q.; Xie, G.; Chen, S.; Gao, S. Lanthanide-Organic Frameworks (LnOFs) Containing 1D Metal/Oxygen Ribbons with Cubane–like and Triangle Motifs: Synthesis, Structure, Luminescence and Slow Magnetic Relaxation. *ChemistrySelect* **2016**, *1*, 3335-3342.

21. Muldoon, P. F.; Collet, G.; Eliseeva, S. V.; Luo, T.-Y.; Petoud, S.; Rosi, N. L. Ship-in-a-Bottle Preparation of Long Wavelength Molecular Antennae in Lanthanide Metal–Organic Frameworks for Biological Imaging. *J. Am. Chem. Soc.* **2020**, *142*, 8776-8781.

22. Chai, H.-M.; Yan, J.-L.; Zhang, G.-Q.; Wang, J.-X.; Ren, Y.-X.; Gao, L.-J. Five Mesoporous Lanthanide Metal–Organic Frameworks: Syntheses, Structures, and Fluorescence Sensing of Fe^{3+}, $Cr_2O_7^{2-}$, and H_2O_2 and Electrochemical Sensing of Trinitrophenol. *Inorg. Chem.* **2022**, *61*, 7286-7295.

23. Schuetz, S. A.; Day, V. W.; Clark, J. L.; Belot, J. A. Direct synthesis of a tetranuclear erbium(III) hydroxo cluster bearing a saturated Schiff base. *Inorg. Chem. Commun*. **2002**, *5*, 706-710.

24. Plakatouras, J. C.; Baxter, I.; Hursthouse, M. B.; Malik, K. M. A.; McAleese, J.; Drake, S. R. Synthesis and structural characterisation of two novel Gd^{III}β-diketonates $[Gd_4(\mu_3\text{-}OH)_4(\mu_2\text{-}H_2O)_2(H_2O)_4(hfpd)_8]\cdot 2C_6H_6\cdot H_2O$ 1 and $[Gd(hfpd)_3(Me_2CO)(H_2O)]$ 2 (hfpd–H = 1,1,1,5,5,5-hexafluoropentane-2,4-dione). *J. Chem*. *Soc*., *Chem*. *Commun*. **1994**, 2455-2456.

25. Lanthanide and Actinide Chemistry (Ed. S. Cotton), Wiley, Chichester, 2006.

26. Wang, Y; Ling, L.; Zhang, W.; Guo, J.; Ding, K.; Duan, W.; Liu, B. "Ship-in-Bottle" Strategy to Encapsulate Shape-Controllable Metal Nanocrystals into Metal–Organic Frameworks: Internal Space Matters. *Chem*. *Mater*. **2019**, *31*, 9546-9553.

27. Corma, A.; Garcia, H. Supramolecular host-guest systems in zeolites prepared by ship-in-a-bottle synthesis. *Eur*. *J. Inorg*. *Chem*. **2004**, *2004*, 1143-1164.

28. Moller, K.; Bein, T. Inclusion chemistry in periodic mesoporous hosts. *Chem*. *Mater*. **1998**, *10*, 2950-2963.

29. Yoshinari, N.; Meundaeng, N.; Tabe, H.; Yamada, Y.; Yamashita, S.; Nakazawa, Y.; Konno, T. Single-Crystal-to-Single-Crystal Installation of $Ln_4(OH)_4$ Cubanes in an Anionic Metallosupramolecular Framework. *Angew. Chem. Int. Ed*. **2020**, *59*, 18048-18053.

30. Konno, T.; Nakamura, K.; Okamoto, K.-I.; Hidaka, J. Preparation and Some Properties of Linear-Type S-Bridged $Ir^{III}Co^{III}Ir^{III}$ Trinuclear Complexes with 2-Aminoethanethiolate (aet) or

L-Cysteinate (L-cys). Crystal Structure of ΔΛ-[Co{Ir(aet)$_3$}$_2$](NO$_3$)$_3$. *Bull. Chem. Soc. Jpn.* **1993**, *66*, 2582-2589.

31. Kawaguchi, S.; Takemoto, M.; Osaka, K.; Nishibori, E.; Moriyoshi, C.; Kubota, Y.; Kuroiwa, Y.; Sugimoto, K. High-throughput powder diffraction measurement system consisting of multiple MYTHEN detectors at beamline BL02B2 of SPring-8. *Rev. Sci. Instrum.* **2017**, *88*, 085111.

32. Macrae, C. F.; Sovago, I.; Cottrell, S. J.; Galek, P. T. A.; McCabe, P.; Pidcock, E.; Platings, M.; Shields, G. P.; Stevens, J. S.; Towler, M.; Wood, P. A. Mercury 4.0: from visualization to analysis, design and prediction. *J. Appl. Cryst.* **2020**, *53*, 226-235.

33. RAPID-AUTO. Rigaku Corporation, Tokyo, Japan.

34. CrysAlisPRO, Oxford Diffraction /Agilent Technologies UK Ltd, Yarnton, England.

35. Sheldrick, G. M. A short history of SHELX. *Acta Cryst.* **2008**, *A64*, 112-122.

36. Sheldrick, G. M. Crystal structure refinement with SHELXL. *Acta Cryst.***2015**, *C71*, 3-8.

37. Dolomanov, O. V.; Bourhis, L. J.; Gildea, R. J.; Howard, J. A. K.; Puschmann, H. J. OLEX2: A complete structure solution, refinement and analysis program. *J. Appl. Cryst.* **2009**, *42*, 339-341.

38. Konno, T.; Okamoto, K.; Hidaka, J. Synthesis and properties of T-cage-type S-bridged rhodium(III)zinc(II) octanuclear complexes with 2-aminoethanethiolate of L-cysteinate. *Inorg. Chem.* **1994**, *33*, 538-544.

39. Yoshinari, N.; Yamashita, U.; Konno, T. A 1 : 1 intercluster compound consisting of +6 and −6 charged $Rh^{III}_4Zn^{II}_4$ octanuclear cations and anions with aminothiolate ligands. *CrystEngComm*, **2013**, *15*, 10016-10019.

40. Yoshinari, N.; Yamashita, S.; Fukuda, Y.; Nakazawa, Y.; Konno, T. Mobility of hydrated alkali metal ions in metallosupramolecular ionic crystals. *Chem*. *Sci*. **2019**, *10*, 587-593.

41. Shannon, R. D. Revised effective ionic radii and systematic studies of interatomic distances in halides and chalcogenides. *Acta Cryst*. **1976**, *A32*, 751-767.

42. The positions of water molecules of crystallization were not fully determined because of their high disorder in crystal.

43. The insolubility of $K_6[\mathbf{1^{Ir}}]\cdot n H_2O$ in ethanol-H_2O (3:1) was confirmed by the absorption spectral measurement.

44. The lanthanide element involved in each of $\mathbf{2_{Ln}}$/$\mathbf{3_{Ln}}$ was specified by the X-ray fluorescence spectroscopy (Figure S14).

45. The cell volumes of $\mathbf{2_{Ln}}$/$\mathbf{3_{Ln}}$, which are almost constant regardless of lanthanide ions involved, are quite similar to the cell volume of $K_6[\mathbf{1^{Ir}}]$ because the cell volumes are governed by the 3D hydrogen-bonded frameworks made up of $[\mathbf{1^{Ir}}]^{6-}$ anions, which are essentially the same as the framework in $K_6[\mathbf{1^{Ir}}]$.

46. Baskar, V.; Roesky, P. W. Lanthanide hydroxide cubane clusters anchoring ferrocenes: model compounds for fixation of organometallic fragments on a lanthanide oxide surface. *Dalton Trans*. **2006**, 676-679.

47. R. L. Carlin, *Magnetochemistry*, Springer, N.Y., 1986, Chap. 9.

48. Van Vleck, J. H.; Frank, A. The Effect of Second Order Zeeman Terms on Magnetic Susceptibilities in the Rare Earth and Iron Groups. *Phys*. *Rev*. **1929**, *34*, 1494-1496.

49. Chilton, N. F.; Anderson, R. P.; Turner, L. D.; Soncini, A.; Murray, K. S. PHI: a powerful new program for the analysis of anisotropic monomeric and exchange-coupled polynuclear d- and f-block complexes. *J. Comput*. *Chem*. **2013**, *34*, 1164-1175.

50. Rohde, A.; Urland, W. Synthesis, crystal structures and magnetic behaviour of dimeric and tetrameric gadolinium carboxylates with trichloroacetic acid *Dalton Trans*. **2006**, 2974-2978.

51. Chandrasekhar, V.; Hossain, S.; Das, S.; Biswas, S.; Sutter, J.-P. Rhombus-Shaped Tetranuclear [Ln_4] Complexes [Ln = Dy(III) and Ho(III)]: Synthesis, Structure, and SMM Behavior. *Inorg. Chem.* **2014**, *53*, 3417-3426.

52. Rasamsetty, A.; Das, C.; Sañudo, E. C.; Shanmugam, M.; Baskar, V. Effect of coordination geometry on the magnetic properties of a series of Ln_2 and Ln_4 hydroxo clusters. *Dalton Trans*. **2018**, *47*, 1726-1738.

53. Rodnyi, P. A.; Khodyuk, I. V. Optical and luminescence properties of zinc oxide (Review). *Opt*. *Spectrosc*. **2011**, *111*, 776-785.

54. Sandmann, A.; Kompch, A.; Mackert, V.; Liebscher, C. H.; Winterer, M. Interaction of L-Cysteine with ZnO: Structure, Surface Chemistry, and Optical Properties. *Langmuir* **2015**, *31*, 5701-5711.

55. van Dijken, A.; Meulenkamp, E. A.; Vanmaekelbergh, D.; Meijerink, A. The Kinetics of the Radiative and Nonradiative Processes in Nanocrystalline ZnO Particles upon Photoexcitation. *J. Phys. Chem. B* **2000**, *104*, 1715-1723.

56. Chen, X.; Wang, Q.; Wang, X.-J.; Li, J.; Xu, G.-B. Synthesis and performance of ZnO quantum dots water-based fluorescent ink for anti-counterfeiting applications. *Sci. Rep.* **2021**, *11*, 5841.

57. Ren, T.-B.; Xu, W.; Zhang, W.; Zhang, X.-X; Wang, Z.-Y.; Xiang, Z.; Yuan, L.; Zhang, X.-B. A General Method To Increase Stokes Shift by Introducing Alternating Vibronic Structures. *J. Am. Chem. Soc.* **2018**, *140*, 7716-7722.

58. Goo, Z. L.; Minami, K.; Yoshinari, N.; Konno, T. Heterometallation of Photoluminescent Silver(I) Sulfide Nanoclusters Protected by Octahedral Iridium(III) Thiolates. *Chem. Asian J.* **2021**, *16*, 2641-2647.

59. Binnemans, K. Interpretation of europium(III) spectra. *Coord. Chem. Rev.* **2015**, *295*, 1-45.

60. Sontakke, A. D.; Biswas, K.; Annapurna, K. Concentration-dependent luminescence of Tb^{3+} ions in high calcium aluminosilicate glasses. *J. Lumin.* **2009**, *129*, 1347-1355.

61. Bünzli, J.-C. G.; Piguet, C. Taking advantage of luminescent lanthanide ions. *Chem. Soc. Rev.* **2005**, *34*, 1048-1077.

SYNOPSIS

Single-crystal-to-single-crystal exchange of K^+ ions in the complex salt of $K_6[Ir_4Zn_4O(L\text{-cysteinate})_{12}]$ ($K_6[\mathbf{1^{Ir}}]$) by Ln^{3+} ions produced 3D coordination polymers consisting of $[Ln_4(OH)_4(OAc)_3(H_2O)_4]^{5+}$ and $[\mathbf{1^{Ir}}]^{6-}$ for the lanthanide series later than Sm^{3+}; these compounds showed solid-state magnetic and photoluminescence properties characteristic of discrete Ln^{3+} species.